JMEPEG (2016) 25:5289–5301
DOI: 10.1007/s11665-016-2368-x

1059-9495/$19.00

Modification of the $Ti_{40}Cu_{36}Zr_{10}Pd_{14}$ BMG Crystallization Mechanism with Heating Rates 10-140 K/min

T. Czeppe, A. Sypien, and A. Wierzbicka-Miernik

(Submitted April 18, 2016; in revised form June 21, 2016; published online October 24, 2016)

The article presents investigations of $Ti_{40}Cu_{36}Zr_{10}Pd_{14}$ bulk metallic glass crystallization process heated with the rates of 10, 60, 100 and 140 K/min. High heating rates experiments were performed in a new type of differential scanning calorimeter equipped with a fast responding thermal sensor. Phase composition and microstructure were studied with x-ray diffraction and transmission electron microscopy. The observed crystallization proceeded in two separate steps. Applied high rates of heating/cooling resulted in the crystallization of only one CuTi phase, replacing typical multi-phase crystallization. The microstructure after crystallization was polycrystalline with some amount of amorphous phase retained. Kinetic parameters were determined with the use of the Kissinger and Friedman iso-conversional analysis and Matusita–Sakka iso-kinetic model. The kinetic analysis supplies results concerning autocatalytically activated mechanism of primary crystallization with decreasing activation energy and small density of quenched-in nuclei, in good agreement with previous structural investigations. The mechanism of secondary crystallization required dense nuclei site, increasing activation energy and large nucleation frequency. The amorphous phase of $Ti_{40}Cu_{36}Zr_{10}Pd_{14}$ BMG revealed high thermal stability against crystallization. Application of high heating rates in DSC experiments might be useful for the determination of mechanism and kinetic parameters in investigations of metallic glasses crystallization, giving reasonable results.

Keywords bulk metallic glasses, crystallization, high heating rates DSC, kinetic parameters, phase composition

1. Introduction

Metallic glasses remain a current subject of the investigations in material sciences. Especially bulk metallic glasses, requiring relatively low critical cooling rates to form amorphous phase, are promising materials for some applications (Ref 1). A lot of attention has been given to finding amorphous equivalents of Al- and Ti-based light alloys. The Ti-based crystalline alloys are characterized by high specific strength and low density. Another important property of both crystalline and amorphous Ti alloys is their biocompatibility which enables their application as different types of implants (Ref 2-4). The mechanical properties of BMGs may be better adapted to parameters required for human implants than those of crystalline alloys (Ref 5).

The $Ti_{40}Zr_{10}Cu_{40-x}Pd_{10+x}$ amorphous alloys were identified as bio-acceptable metallic glasses (Ref 1, 5, 6). The Pd compositions of 10, 14 and 20 at.% were first invented by the Inoue group and later widely studied (Ref 7-9). The BMGs reveal quite wide supercooled liquid range ΔT, between glass transition T_g and primary crystallization temperature T_{x1}, and good glass-forming ability (GFA). Most of the published investigations concentrated on the alloys with 14 at.% of Pd, because of high glass-forming ability and large critical diameter available (Ref 5). Further development of TiZrCuPd alloys focused on attempts to increase the critical diameter of bulk glassy samples by small additions of the other element, preserving their biocompatibility. Small amounts of Sn (Ref 5, 7) and Nb were investigated (Ref 10). The small Nb content successfully improved the strength of the alloys but also promoted the precipitation of the composition-dependent Pd_3Ti phase.

From the point of view of application, the main weakness of BMGs as a constructive material remains poor deformability at room temperature in the range of heterogeneous deformation. However, formability may be good in the supercooled liquid range, in which metallic glasses may deform by homogenous flow mechanism (Ref 11). The precise knowledge of crystallization mechanism of particular BMG, including nucleation and growth, is important for the perspective of applications.

The crystallization mechanism of TiZrCuPd BMGs with 10-20 at.% Pd is quite complex, including at least two stages, primary and secondary crystallizations. After completed crystallization, the phases were identified as Cu_8Zr_3 and Cu_4Ti_3 (Ref 5) or Cu_8Zr_3, CuTi and $PdTi_2$ (Ref 7). However, the phases identification based on XRD is not easy due to large number of lines in the patterns and a low symmetry of the phases. Small additions of Sn and Nb further modify the crystallization mechanism (Ref 5, 7, 10). Moreover, the issue of microstructure and phase composition after primary crystallization remains unclear. It was shown in Ref 12, in that the primary crystallization of the $Ti_{40}Zr_{10}Cu_{40}Pd_{10}$ glassy alloy proceeded by diffusion of Ti and Cu between amorphous and crystalline phases and the formation of 1-2 nm clusters growing into 5-nm crystallites, identified as Cu_8Zr_3, Cu_2Ti and Cu_3Pd phases. After the primary crystallization, a large part of the amorphous phase may be retained, even after the relatively long annealing time of 600 s at 750 K temperature (Ref 13). High-resolution microscopy (HREM) shows that the amorphous phase separates into two slightly different compositions (Ref

T. Czeppe, A. Sypien, and **A. Wierzbicka-Miernik,** Institute of Metallurgy and Materials Sciences PAS, 25 Reymonta St., 30-059 Kraków, Poland. Contact e-mail: t.czeppe@imim.pl.

13) which should influence the primary crystallization process as well. Thermo-mechanical analysis, conducted with small constant loads and at 5 K/min heating rate, confirmed that due to the large part of the retained amorphous phase, deformation by the homogenous flow also overlapped the temperature range of primary crystallization (Ref 13).

The process of amorphous alloys crystallization is usually studied with differential scanning calorimetry (DSC), in continuous heating regime with relatively high rates β, from 20 to 40 K/min. Slower heating rates may cause preliminary nano-crystallization in the supercooled liquid temperature range. Phase composition observed after DSC cycle may also be influenced by diffusion processes which undergo during relatively slow cooling of the calorimeter. The DSC experiments enable the determination of kinetic parameters, commonly the activation energy E_a for nucleation and crystallization. The activation energy for primary crystallization of the $Ti_{40}Zr_{10}Cu_{36}Pd_{14}$ BMG was determined to be 287.6 kJ/mol (Ref 7).

New types of DSC calorimeters, equipped with fast responding thermal sensors enabling much faster heating and cooling, are now available. Such equipment was applied to study the crystallization process of the $Ti_{40}Cu_{36}Zr_{10}Pd_{14}$ BMG with DSC measurements performed at high rates of heating and cooling, 60, 100 and 140 K/min. Also the x-ray phase analysis (XRD) and transmission electron microscopy (TEM) were used in order to compare the results with the mechanism of crystallization deduced from the experiment performed with relatively small heating rate 10 K/min and suggested by results presented in the papers (Ref 12-14).

Simple methods of kinetic parameters determination widely used in the literature concerning metallic glasses were applied for the interpretation of DSC results. The results of the activation energy E_a were calculated by the Kissinger and Friedman methods. Also, the non-iso-conversional kinetic method of Matusita–Sakka, frequently used in case of metallic glasses, was applied, in spite of the fact that the method was invented for very slow processes of crystallization proceeding in $Li_2O{\cdot}2SiO_2$ glasses (Ref 15, 16). The intention of the authors was to verify whether the models might give reasonable results in the case of high rates of heating used in part of the DSC experiments.

2. Materials and Methods

Master alloy of nominal composition $Ti_{40}Cu_{36}Zr_{10}Pd_{14}$ was prepared by cold crucible levitation melting under a high-purity argon atmosphere (Ref 17). The glass samples were prepared by cooper mold injection casting method. They were 3 mm in diameter and 40 mm long. All samples were amorphous, as confirmed by XRD, TEM and HREM.

The transition of glass into crystalline morphology was studied in DSC calorimeters. The DSC Netzsch 214 Polyma was used for the experiments with the heating and cooling rates β 60, 100 and 140 K/min. The Netzsch DSC 214 has a new construction and is equipped with the fast responding thermal sensor enabling registration of the heat flux with high heating rates up to the temperature of 900 K. The DSC experiment with β 10 K/min was performed using another calorimeter, Netzsch DSC F1 Pegasus. The calorimeters were calibrated according to the Netzsch calibration procedure. The temperature calibration

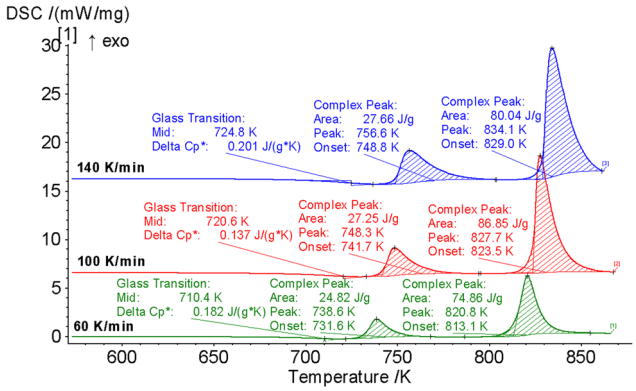

Fig. 1 DSC curves for the Ti40Cu36Zr10Pd14 BMG, applied heating rates β: 60, 100 and 140 K/min. The DSC Netzsch 214 Polyma

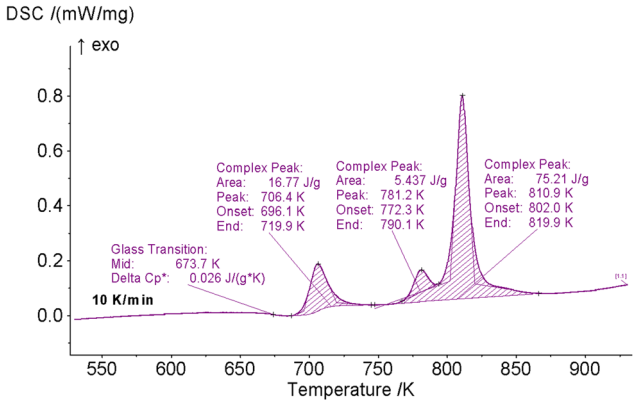

Fig. 2 DSC curves for the Ti40Cu36Zr10Pd14 BMG, applied low heating rate 10 K/min. DSC Netzsch F1 Pegasus

was performed through the melting of the 4 or 5 commonly used standards, In, Sn, Zn, Al and Ag for each heating rate separately in case of the DSC F1 Pegasus. Cell constants were determined from the Zn heat of fusion, calculated from each heating rate. Samples with mass of about 30 mg were used in the form of disks, 3 mm in diameter and about 2 mm in height. The Cu pans were used to improve the thermal contact of the samples with the calorimeter and as standards. The measurements were taken in an atmosphere of high-purity argon.

The microstructure and phase composition after crystallization were determined with x-ray diffraction (XRD) and transmission electron microscopy (TEM). For the XRD measurements, the D2 Phaser (Brukers) with X Flash detector and Cu K_α radiation was used. TEM experiments were performed with the electron microscope TECNAI (FEI, G2 FEG/200 kV) equipped with the EDAX Phoenix system for microanalysis.

3. Results

3.1 Results of DSC Experiments

The DSC curves of the BMG crystallized with heating rates of 60, 100 and 140 K/min are presented in Fig. 1 and with low heating rate 10 K/min in Fig. 2. The characteristic temperatures

and enthalpies determined from the DSC are presented in Table 1. In the case of high heating rates, the crystallization was manifested by two exothermic effects preceded by an endothermic one resulting from glass transition and heat capacity increase in the supercooled liquid range, ΔT. Since crystallization is a diffusion-controlled process, peak temperatures T_p increased together with the increase in the heating rates. In effect, the second thermal effect could not be completely registered for the rate of 140 K/min, approaching the temperature limit of the Netzsch DSC 214 Polyma. Kinetic models requiring complete peak shape could not be applied for this peak. It may be noticed that the first exothermic peak related to primary crystallization at the high-temperature side reveals broadening, which may be related to a prolonged, relatively slow crystallization process or/end large thermal lag, while the secondary crystallization peak is much narrower and

Table 1 Characteristic temperatures of glass transition (T_g), crystallization (T_x), peak temperature (T_p), supercooled liquid range (ΔT), and enthalpies (ΔH) determined from the DSC curves

Heating rates, K/min	T_g, K	T_{x1}, K	ΔT, K	T_{p1}, K	ΔH_1, J/g	T_{x2}, K	T_{p2}, K	ΔH_2, J/g
10	674.0	696.0	22	706.0	17.0	802.0	811.0	75.0
60	710.0	732.0	22	739.0	25.0	813.0	821	75.0
100	721.0	742.0	21	748.0	27.0	824.0	828.0	87.0
140	725.0	749.0	24	757.0	28.0	829.0	834.0	…

Indexes 1 and 2 denote the first and the second exothermic peaks related to the primary and secondary crystallizations of the BMG.

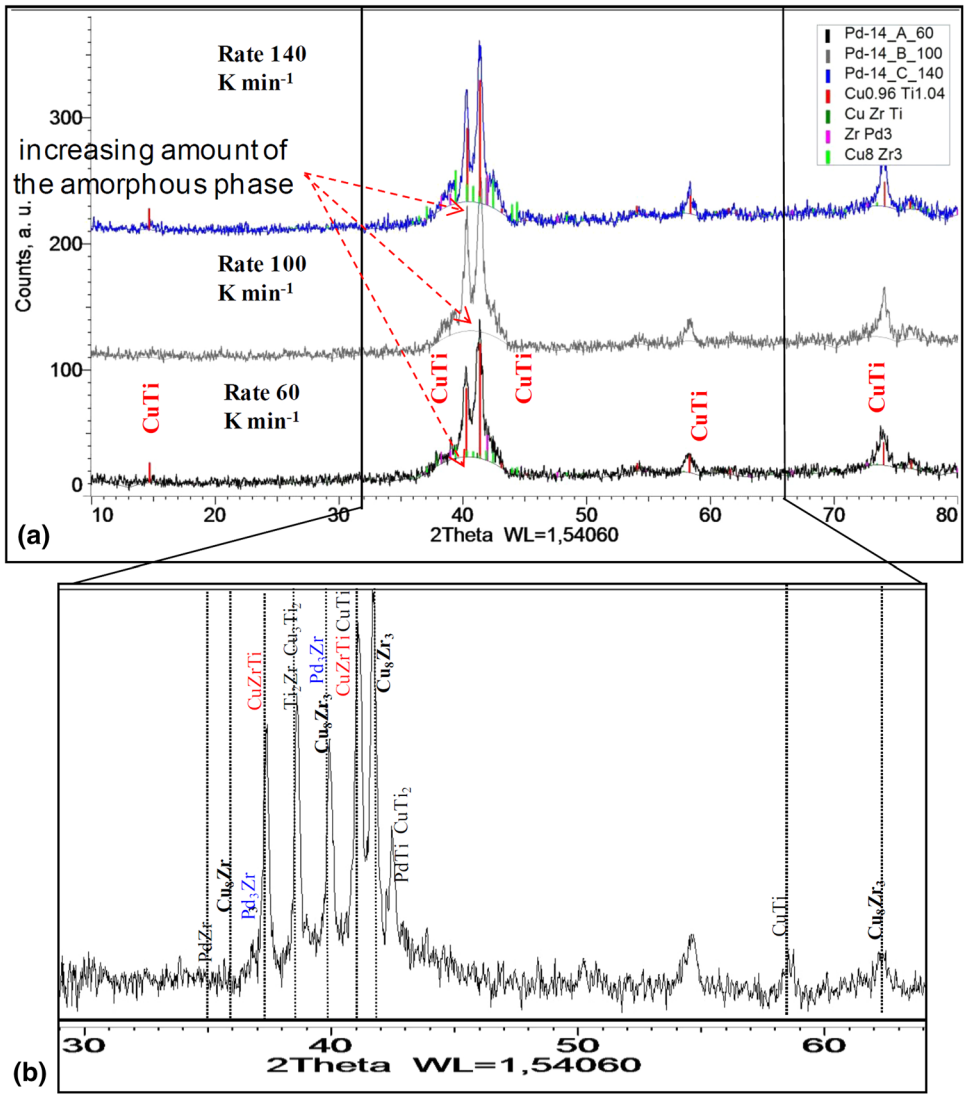

Fig. 3 XRD pattern after complete crystallization in DSC, heated up to 900 K, at rate β (a) 20 K/min, (b) 60, 100 and 140 K/min

symmetrical. The last observation suggests a single crystallization event. The enthalpy increase in the primary crystallization (Table 1) brought about by the rise of the heating rate from 100 to 140 K/min is very small, not exceeding 1%, while the difference in enthalpy between the crystallization proceeding with the rates 60 and 100 K/min is much larger, about 10% (Table 1). The different sensitivity of the first and the second steps of crystallization for increasing heating rates suggests the different character of the respective crystallization mechanisms.

The DSC curve of the BMG crystallization process with the heating rate 10 K/min is shown in Fig. 2. It is visible that except two thermal effects mentioned previously, an additional one is present at 772 K temperature. It is slightly lower than the start temperature of the secondary crystallization T_{x2}. Results presented in Table 1 show that in spite of the wide range of heating rates the supercooled liquid temperature range ΔT remains nearly constant, the enthalpy of primary crystallization is similar for high heating rates but lower for β 10 K/min, while enthalpy of the secondary crystallization established from the second exothermic effect remains stable for rates 10-60 K/min. The additional peak observed for β 10 K/min decays in the DSC curves for rates 20 and 30 K/min, not presented here.

3.2 The Structure and Phase Composition After Crystallization

The XRD investigations of phase composition of the samples crystallized in DSC with high rates of heating 60, 100 and 140 K/min proved the great influence of heating rates on the samples' phase composition (Fig. 3a). As opposed to the samples crystallized with low rate (20 K/min) (Fig. 3b), all the diffraction peaks of samples crystallized at high heating rates could be identified as resulting from the presence of a single CuTi phase (Fig. 3a), which is tetragonal with lattice parameters a = 3.115 and c = 5.947 (Ref 18). Except the crystalline phase, large intensities observed at about 2Θ-40° and increasing with the heating rate are due to some amount of amorphous phase retained after crystallization. It is visible in Fig. 3(b) that crystallization with the rate of β—20 K/min leads to the appearance of many other phases apart from the CuTi phase. They were identified as $CuTi_2$, Cu_3Ti_2, Cu_8Zr_3 (orthorhombic, a = 7.869, b = 8.147, c = 9.977), PdTi, PdZr, Pd_3Zr (hexagonal, a = 5.611, c = 9.232) and Ti_2Zr. Also, some evidence for the presence of ternary CuZrTi phase (tetragonal, a = 3.097, c = 11.036) exists. The phases Cu_8Zr_3 and CuTi are especially well documented in the literature (Ref 5, 7).

The TEM microstructures of the samples after crystallization, heated with the rates of 60 and 140 K/min, are shown in Fig. 4. The morphology was very similar, except that lighter crystals and smaller average dimensions of the grains were noticed in the case of the sample heated with β 140 K/min. The electron diffraction patterns for both samples are shown in Fig. 5. They reveal strongly polycrystalline character, while the first rings of intensity, very intensive and widened, suggest some amount of amorphous phase retained after crystallization. In both cases, all calculated d_{hkl} distances between crystalline planes fit the CuTi phase (Fig. 5). No other phases were identified in TEM investigations.

HREM microstructures shown in Fig. 6(a) and (b) present crystalline particles in the amorphous matrix identified by the fast Fourier transform (FFT) as CuTi phase, always observed with common orientation [100] or [221] (Fig. 6c, d, e and f).

The example of the microstructure of the individual CuTi crystalline particle is shown in Fig. 7(a), together with the corresponding SADP (Fig. 7b) with the [100] zone axis of the lattice, revealing a monocrystalline type of electron diffraction.

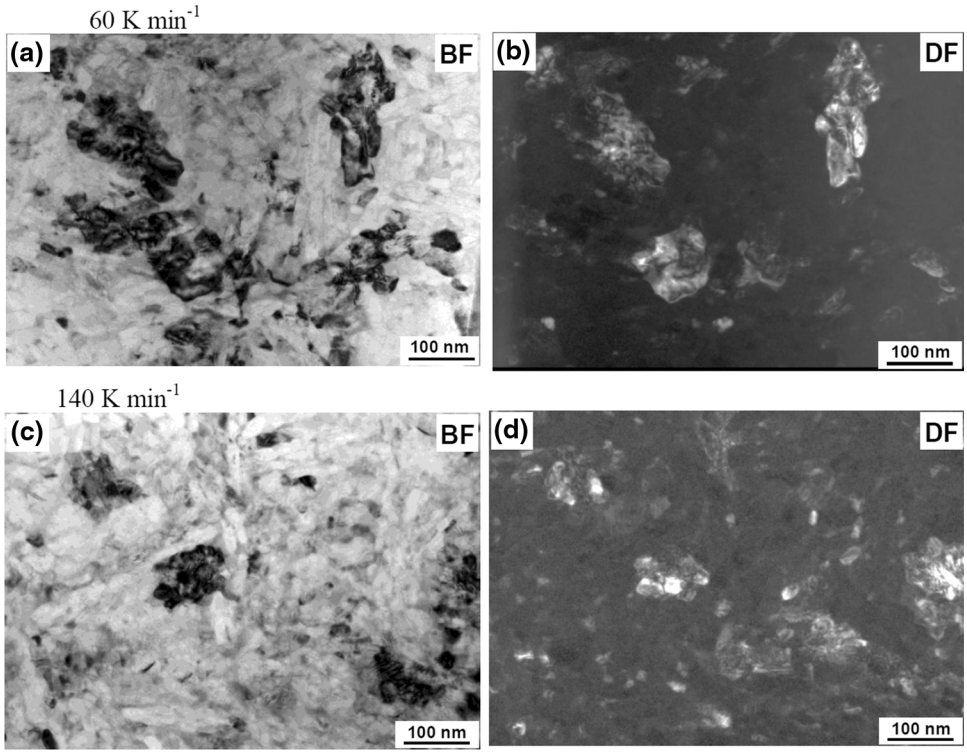

Fig. 4 TEM microstructures of samples crystallized in DSC at rates: 60 K/min (a) bright-field (BF) technique, (b) dark-field (DF) technique; 140 K/min (c) (BF), (d) (DF)

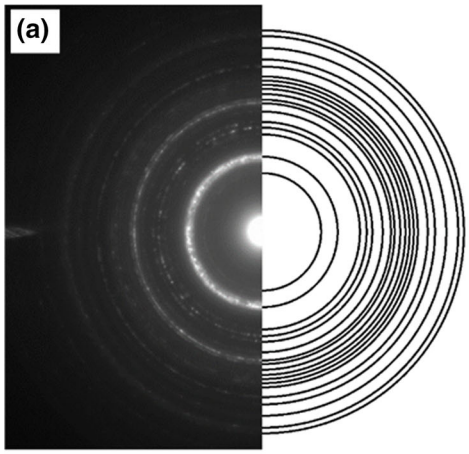

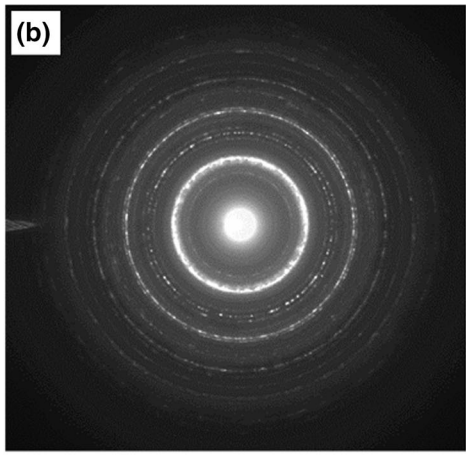

R	d [A]	I [%]	CuTi h,k,l
113	2.804	41	101
145	2.180	100	110, 102
188	1.687	29	103
201	1.580	34	200
212	1.498	29	004
232	1.369	28	*202, 211*
248	1.279	46	212
255	1.245	34	114
266	1.192	25	005
276	1.151	24	*213*
284	1.118	24	105
292	1.089	24	221,204
300	1.057	21	115
319	0.996	22	006, 310, 302
333	0.954	18	205, 106
355	0.895	18	116, 215, 224
378	0,840	18	322
389	0.816	16	314, 107

R	d [A]	I [%]
113	2.801	46
146	2.176	100
188	1.686	34
201	1.580	41
212	1.499	33
232	1.370	31
248	1.278	53
255	1.244	38
266	1.195	28
276	1.151	28
284	1.117	28
292	1.088	28
300	1.057	24
319	0.995	27
333	0.954	21
355	0.895	21
378	0.840	22
390	0.815	19

Fig. 5 Comparison of the selected area diffraction patterns of the samples crystallized in DSC at rates (a) 60 K/min, (b) 140 K/min. All d_{hkl} lattice confirms the appearance of CuTi phase

The XRD and TEM results proved a large difference between the crystallization mechanisms of the $Ti_{40}Cu_{36}Zr_{10}Pd_{14}$ BMG with the heating rates β from 60 to 140 K/min, compared with the commonly used rate β 20 K/min. The crystallization process proceeding with high heating rates proved to be much simpler, reduced only to the single, CuTi phase, replacing multiphase crystallization at lower heating rates β 10-30 K/min, commonly presented in the literature (Ref 5, 7). At the same time, a noticeable amount of the amorphous phase was retained. The main difference between the microstructures of the samples crystallized with the heating rates 60 and 140 K/min was larger dispersion of the crystalline particles in the case of the higher heating rate.

3.3 Kinetic Parameters of Crystallization

Activation energy E_a is one of the basic kinetic parameters useful for the description of metallic glasses crystallization. The value of E_a may depend on the transformed fraction, which means that the crystallization mechanism represented by respective peaks in the DSC curve undergoes modification. Determination of E_a also enables establishing another valuable parameter, which is nucleation frequency Z_{nf} (Ref 19, 20). It is assumed that nucleation and growth processes participate in both steps of crystallization of the experimentally detected CuTi phase. The activation energy E_a was determined with the Kissinger and Friedman methods.

The Kissinger method (Ref 21) takes into account only peak temperature T_p and heating rate β. The results for the primary and secondary crystallizations, for the heating rates 60, 100 and 140 K/min, are presented in the first row of Table 2. The activation energy E_a of the primary crystallization was determined to be 218 kJ/mol. For the secondary crystallization, E_a was slightly larger, 352 kJ/mol. It was interesting to verify whether the E_a value may be consistently determined using a small heating rate such as 10 K/min, as well (Fig. 2; Table 1). The $\ln(\beta/T_p^2) = f(T_p^{-1})$ relation, shown in Fig. 7, used for the determination of E_a in Kissinger method remains linear, giving possibility for the determination of activation energy for all, small and large heating rates with a good fitting parameter of 0.995 or better (Fig. 8; Table 2). The E_a values calculated for all heating rates are larger by 50 kJ/mol than the values

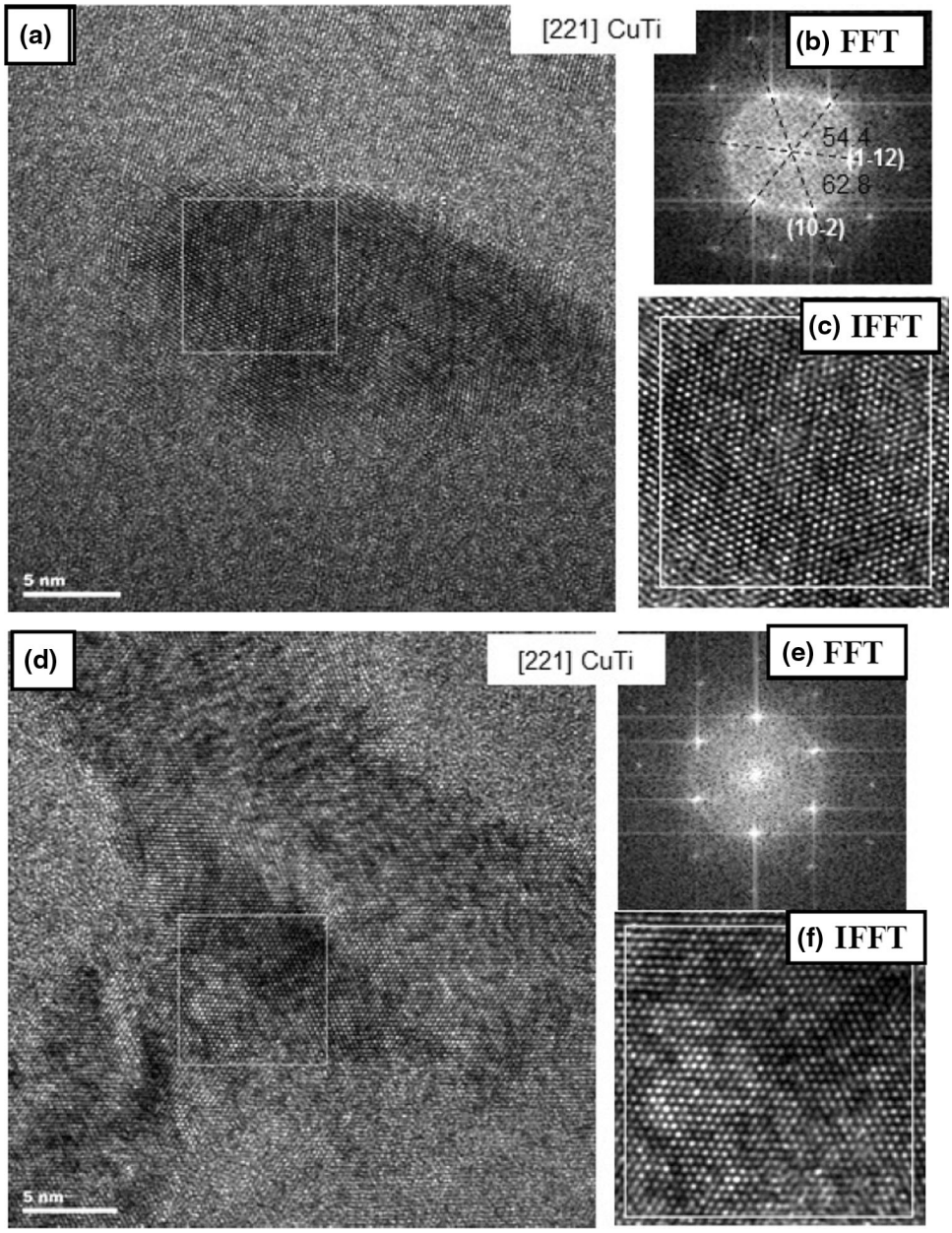

Fig. 6 HREM images, fast Fourier transforms FFT and corresponding IFFT images of the samples crystallized in DSC at rates: 60 K/min (a) image, (b) FFT, (c) IFFT from the selected area; 140 K/min (d) image, (e) FFT, (f) IFFT from the selected area

calculated for only high heating rates in the case of the primary crystallization peak. However, the difference is only 8 kJ/mol for the secondary crystallization peak (Table 2). This suggests a difference in the crystallization mechanism of the primary crystallization proceeding with the small and large β. The nucleation frequency Z_{nf} was calculated with the use of the formula:

$$\beta/T^2 = (Z_{nf}R/E_a)\exp(-E_a/RT) \quad \text{(Eq 1)}$$

where β is the heating rate and R gas constant (Ref 19, 20).

Table 2 shows that the nucleation frequency of the primary crystallization is smaller than of the secondary one and clearly increases from 1.3exp(14) to 4.1exp(17) when small heating rate was included. The nucleation frequency of the secondary crystallization proved to be not sensible to heating rate remaining in the range of (1.7-5.8)exp(21).

The Friedman iso-conversional analysis enables the determination of the relation between transformed fraction d_x and activation energy E_a, from equation (Ref 22):

$$\ln\frac{dx}{dt_{x=xj}} \ln A - \frac{E_a}{RT} + \ln(f_j) \quad \text{(Eq 2)}$$

where dx is the transformed fraction, t time, T temperature, R gas constant and A constant.

Also, in this case the calculations of E_a were done separately for heating rates β 60, 100 and 140 K/min and including the β 10 K/min. The results for primary and secondary crystallizations are presented in Tables 3 and 4 and in Fig. 9 and 10,

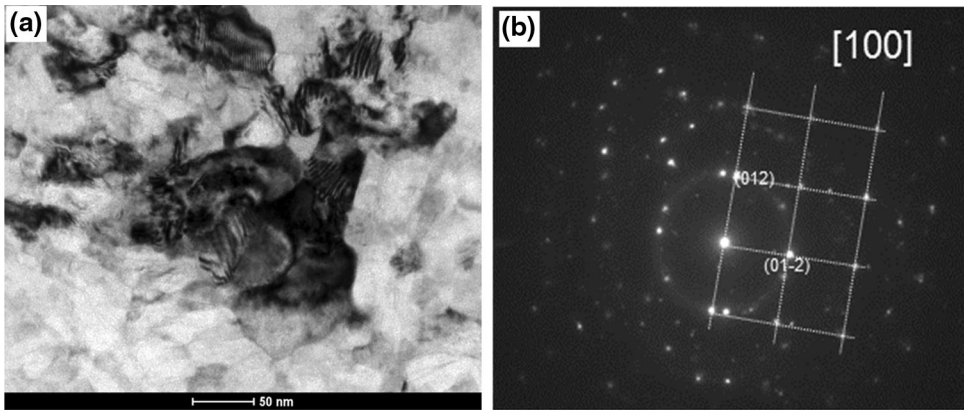

Fig. 7 TEM microstructure of sample crystallized at rate β 60 K/min, micrographs: (a) bright-field image (BF), (b) selected area diffraction (SADP) pattern from the dark particle, CuTi phase, zone axis [100]

Table 2 Activation energy (E_a) at the peak temperature (T_p) and nucleation frequency (Z_{nf}) in dependence on the included heating rates (β)—Kissinger method

Heating rates β K/min	E_a, kJ/mol Peak 1	E_a, kJ/mol Peak 2	Z_{nf}—nucleation frequency Peak 1	Z_{nf}—nucleation frequency Peak 2
60, 100, 140	217.9	352.2	1.28exp(14)	1.71 exp(21)
10, 60, 100, 140	266.9	360.4	4.10exp(17)	5.78 exp(21)

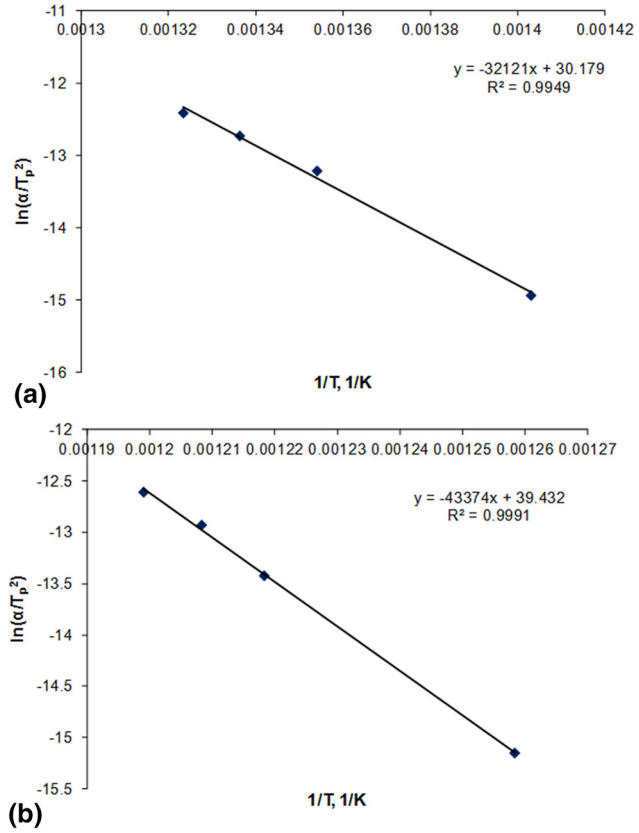

Fig. 8 Determination of the activation energy for crystallization according to Kissinger relation (Ref 21) for primary (a) and secondary crystallizations (b)

while the example of the respective DSC curves and integrated area fractions with dx specific for T_p marked by the arrows for the β 60 K/min between 33 and 26% are presented in Fig. 11.

As results from Friedman method, the activation energy E_a of primary and secondary crystallizations reveals some dependence on the degree of conversion d_x (Tables 3, 4; Fig. 9, 10), which means a complex reaction path. The values of E_a revealed the same dependence on β as achieved by the Kissinger method when low heating rate β 10 K/min was included in the calculations, the values of E_a increased (Fig. 10). However, for the primary crystallization (Fig. 10a) the Friedman analysis revealed the E_a decrease at two different ranges in both methods of E_a calculations. In the first one, the decrease was more rapid, up to the transformed fraction of about 30% (Fig. 11a). In the second range, at larger d_x, E_a decreases very slowly or, in the calculations including only high heating rates, the E_a remains nearly constant (Fig. 10a). Consequently, it may be deduced that the first range of transformation predominantly related to nucleation has the character of an autocatalytically activated reaction. At larger transformed fractions d_x, the nucleation frequency decreases slowly or stabilizes.

A different E_a dependence results from Friedman analysis of the secondary crystallization presented in Fig. 10(b). As demonstrated, the E_a increases up to d_x specific for the T_p, and decreases at higher transformed fractions d_x. The behavior is more pronounced for the crystallization with high heating rates. When low β 10 K/min was considered, the calculated E_a was smaller and its increase more moderate. All this suggests much larger E_a required for the crystallization of only single CuTi phase in comparison with the multi-phase process proceeding with small heating rates.

Table 3 Numerical values of E_a achieved from Friedman analysis for the heating rates (β) 60, 100 and 140 K/min

Partial area	Activation energy E_a, kJ/mol	
	Primary crystallization	Secondary crystallization
0.020	248.98 ± 1.17	287.54 ± 25.33
0.050	241.34 ± 6.64	317.47 ± 21.78
0.100	226.88 ± 15.67	362.36 ± 29.31
0.200	202.18 ± 24.82	465.22 ± 86.75
0.300	182.51 ± 25.10	481.46 ± 43.10
0.400	170.31 ± 20.82	386.26 ± 14.84
0.500	163.57 ± 14.71	301.50 ± 3.33
0.600	159.69 ± 7.78	244.04 ± 22.04
0.700	155.14 ± 0.88	214.41 ± 35.50
0.800	152.51 ± 8.19	209.08 ± 47.15
0.900	167.29 ± 3.43	230.63 ± 63.84
0.950	209.71 ± 7.29	270.42 ± 69.91
0.980	251.51 ± 37.08	356.92 ± 45.21

Table 4 Numerical values of Ea achieved from Friedman analysis for the heating rates (β) 10, 60, 100 and 140 K/min

Partial area	Activation energy E_a kJ/mol	
	Primary crystallization	Secondary crystallization
0.020	389.81 ± 29.95	368.02 ± 19.36
0.050	369.69 ± 28.08	364.77 ± 12.56
0.100	344.95 ± 26.55	360.04 ± 6.84
0.200	309.54 ± 24.77	372.95 ± 28.55
0.300	282.66 ± 23.10	371.55 ± 28.35
0.400	261.48 ± 21.04	340.25 ± 12.48
0.500	243.56 ± 18.60	307.52 ± 1.82
0.600	228.38 ± 16.32	283.59 ± 12.53
0.700	213.01 ± 14.11	269.57 ± 19.07
0.800	198.63 ± 11.50	266.26 ± 24.00
0.900	185.93 ± 2.55	282.25 ± 33.53
0.950	177.41 ± 14.92	310.19 ± 39.48
0.980	190.14 ± 30.85	341.38 ± 24.55

The respective E_a values determined by the Kissinger method at T_p for the primary crystallization (Table 2), marked in Fig. 10(a), revealed values to be in good agreement with those determined from the Friedman analysis, taking into account the respective range of the crystallized fraction. In case of the secondary crystallization, the Kissinger E_a values are underestimated if calculated with high heating rates, but fit very well to the E_a determined from the Friedman analysis calculated taking into account all the heating rates (Table 2; Fig. 10b).

The Matusita–Sakka (Ref 15, 16) method was applied to both steps of crystallization. There are two parameters to be determined: Avrami parameter n and dimensional parameter m, both related by the equation:

$$\ln(-\ln(1-x)) = -n\ln(\beta) - 1.052mE_a/RT + C \qquad \text{(Eq 3)}$$

where x is the transformed fraction, β heating rate, R gas constant and T temperature.

The parameter n is determined as a tangent of the double-logarithmic relation:

$$\ln(-\ln(1-x)) = f(\beta) \text{ for the given } T \qquad \text{(Eq 4)}$$

assuming that a linear relation exists for different heating rates β. For the given heating rate β, the relation:

$$\ln(-\ln(1-x)) = f\left(T^{-1}\right) \qquad \text{(Eq 5)}$$

enables the determination the m parameter (Ref 15, 16). The way in which the parameter n was determined is shown in Fig. 12(a), while the example of the m parameter determination for the heating rate 60 K/min is shown in Fig. 12(b).

The n values determined on the basis of the model are presented in Table 5, for both the primary and secondary crystallizations. As the values vary with temperature, the average values n_{av} 4.8 for the primary crystallization and 3.8 for the secondary crystallization were calculated. According to the model, the dimensional parameter m may take values $n-1$ or $m = n$. The calculated m parameter together with the interpretation is presented in Table 6 for each heating rate and all crystallization steps. It is visible that the n parameter

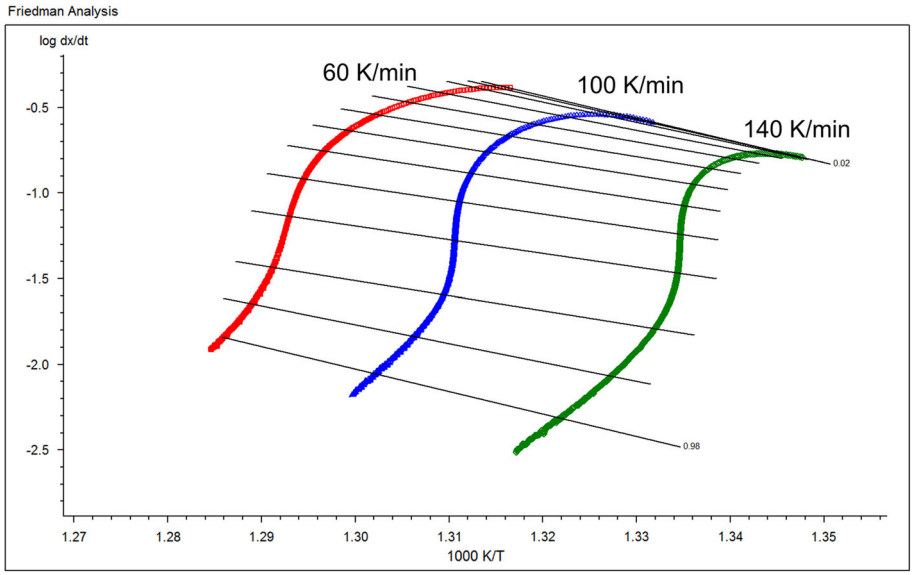

Fig. 9 Friedman analysis for heating rates β 60-140 K/min: the relation between transformation rate dx/dt and reversed temperature ($T-1$), revealing dependence of activation energy E_a upon transformed fraction (Ref 22)

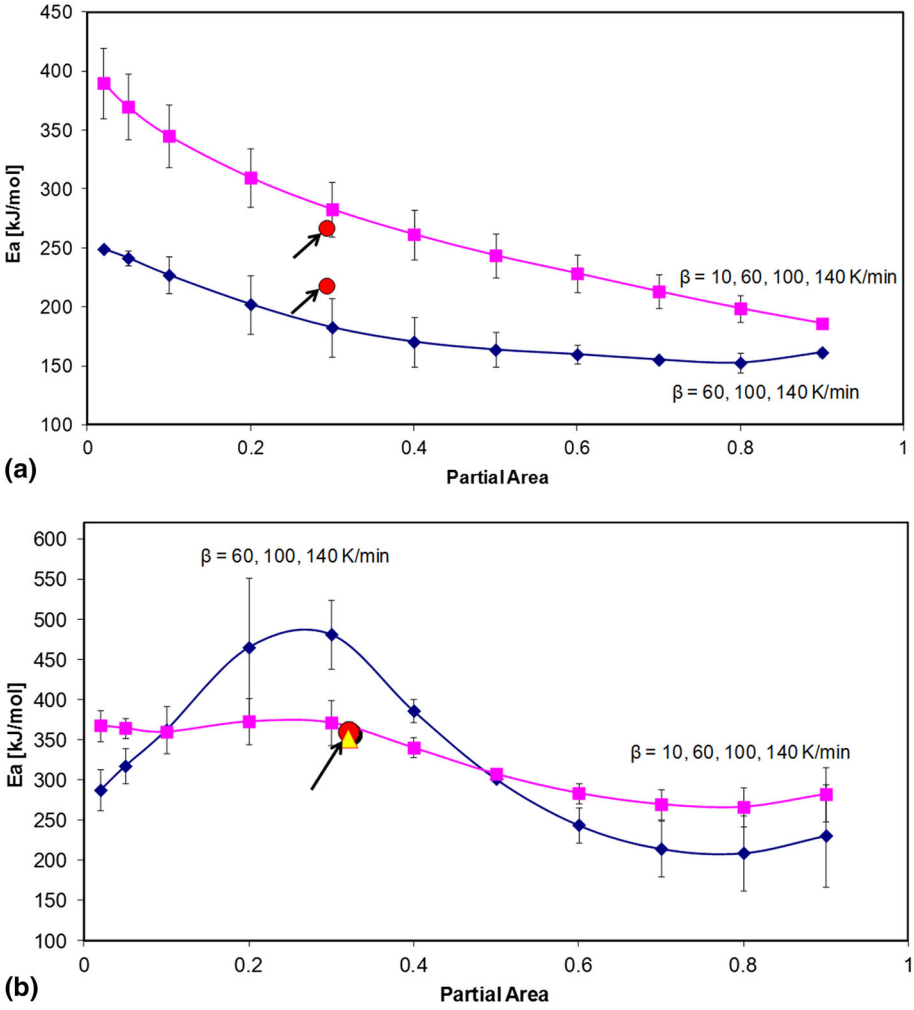

Fig. 10 Friedman analysis: relation between activation energy Ea and transformed fraction dx calculated for heating rates β 10-140 and 60-140 K/min (Ref 19); (a) primary crystallization DSC peak, (b) secondary crystallization DSC peak. The values of the E_a determined by Kissinger method marked by arrows

determined for the first peak of crystallization and heating rate β 60 K/min is too large because the m parameter exceeds 3D. In all other cases, n and m parameters remain reasonable. The crystallizing particles are always three-dimensional. Also, the dense nuclei sites should not appear in the primary crystallization. In the case of the second step of crystallization, the model suggests that the dense nuclei sites are present provided the rates are the highest: 100 and 140 K/min (Ref 15, 16). The results seem to be in a good qualitative agreement with the nucleation frequency Z_{nf}, calculated based on the Kissinger activation energy E_a (Table 2), which is much smaller for the primary than for the secondary crystallization. It should be remembered that the values of Z_{nf} are averaged over all heating rates, while the m parameter of the Matusita-Sakka model is determined for each heating rate separately.

4. Discussion

According to the results from the DSC experiments, low heating rate 10 K/min of the $Ti_{40}Cu_{36}Zr_{10}Pd_{14}$ BMG did not lead to nanocrystallization observed in the supercooled liquid temperature range (Fig. 2). The XRD and TEM results proved that the crystallization process performed with high heating rates from 60 to 140 K/min was simplified. The multi-phase crystallization was replaced by the crystallization of single-phase CuTi. This phase was also suggested previously in case of the CuTiZrPd BMGs crystallization (Ref 7). The result proves that, in thermodynamic terms, the CuTi phase reveals the largest driving force for the nucleation and growth for the investigated composition range of the amorphous alloys. The refinement of the polycrystalline microstructure shown by TEM also revealed its dependence on heating rate. The problem of the selection of crystallizing phases in the case of the metallic glasses is not easy to explain and must be directed to both thermodynamics and kinetics. Because of selected CuTi crystallization at the high heating rates, only some suggestions may be given. Ti and Cu atoms are the main components of the alloy, statistically most probable near neighbors in disordered amorphous matrix which reduces the required diffusion distance. There is no solubility of Cu in Ti, while other components reveal solubility in one of the components, which increases tendency for the intermetallic Cu–Ti phase formation.

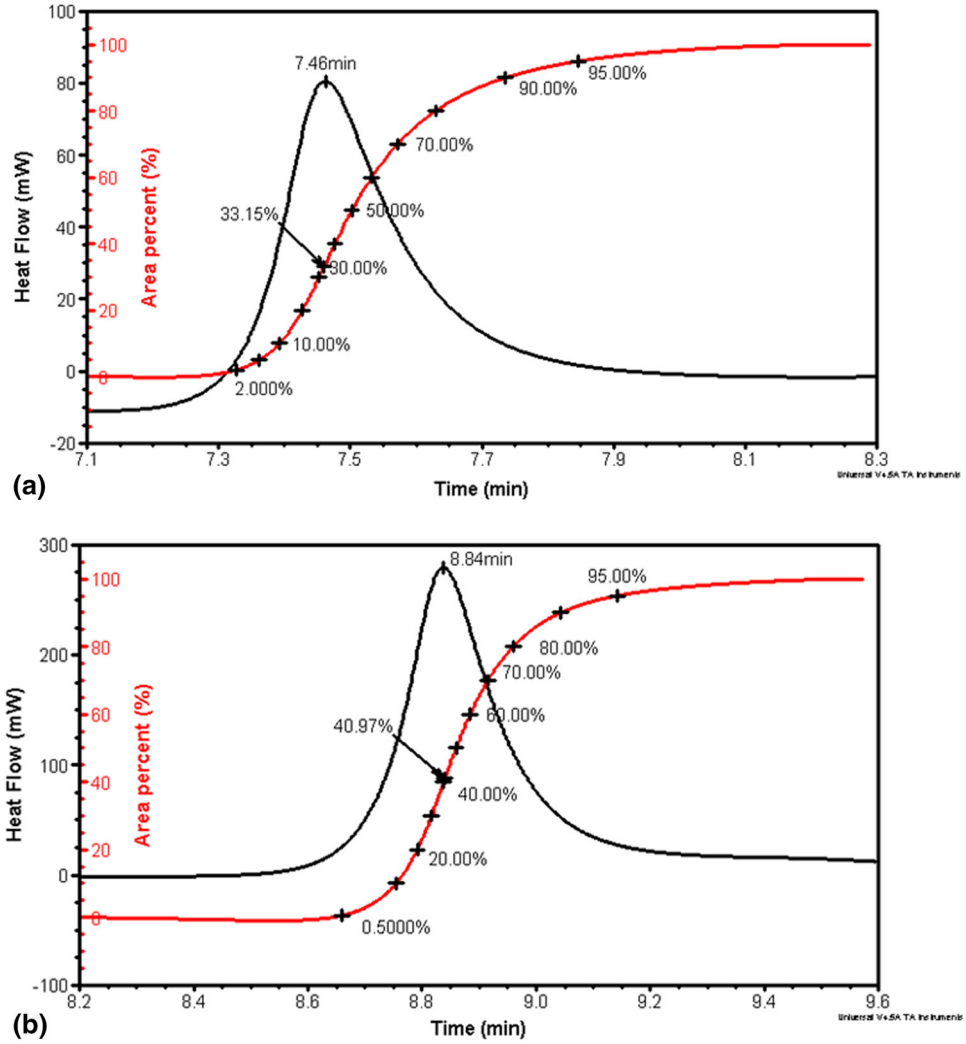

Fig. 11 Relative integrals from the first (a) and the second (b) crystallization peak in the DSC curves, with β = 60 K/min. The fracture crystallized at peak temperature T_p marked by arrow

Also, in many amorphous compositions Cu atoms reveal strong tendency for the clustering in liquid phase. As was shown in case of the FINMET alloy (Ref 26), such clusters are the place for the crystalline phase nucleation. Together with the surrounding Ti atoms, such clusters may play the role of the nuclei in the amorphous matrix. As is visible from the experiments, the nucleation and growth kinetics are going to be decisive at high heating rates.

The activation energy of crystallization and growth E_a, determined with the use of different methods, concerns only CuTi phase which transformed because of the decrease in amorphous phase thermal stability at high heating rates. The E_a is usually determined with Kissinger method (Ref 7, 8, 20, 23). It was revealed that the straight line obtained for the E_a evaluation refers not only to the high heating rates but also to heating rates from 10 to 140 K/min. The values of E_a were calculated both for high heating rates separately and including the heating rate of 10 K/min. Table 2 and Fig. 10(a) show that the E_a determined by Kissinger method is significantly larger for the primary crystallization performed with 10 K/min rate. This means higher activation energy of nucleation when the multi-phase crystallization with the low heating rate proceeds in the primary crystallization range. This also suggests a relation with the nucleation process occurring with much higher frequency Z_{nf}, of multi-phase nucleation. It is not the case when the secondary crystallization is considered, since no significant differences of E_a and Z_{nf} in the calculation by Kissinger method were noticed (Table 2; Fig. 10b).

Essentially, the Kissinger method supplies the E_a values for the fraction transformed at peak temperature T_p, which slightly depends on higher heating rates. This means that E_a values determined by the method are averaged for the transformed fractions between 20 and 40% (Fig. 11). The Friedman method of E_a determination reveals the dependence of E_a on the transformed fraction. Figure 10 shows that E_a of both primary and secondary crystallizations exhibits some dependence on crystallized fraction, which suggests that complicated, autocatalytic mechanism of crystallization is involved (Ref 22). The E_a of the primary crystallization decreases with the transformed fraction, which also indicates the decrease in the nucleation frequency Z_{nf}. Such a behavior fits in well with the

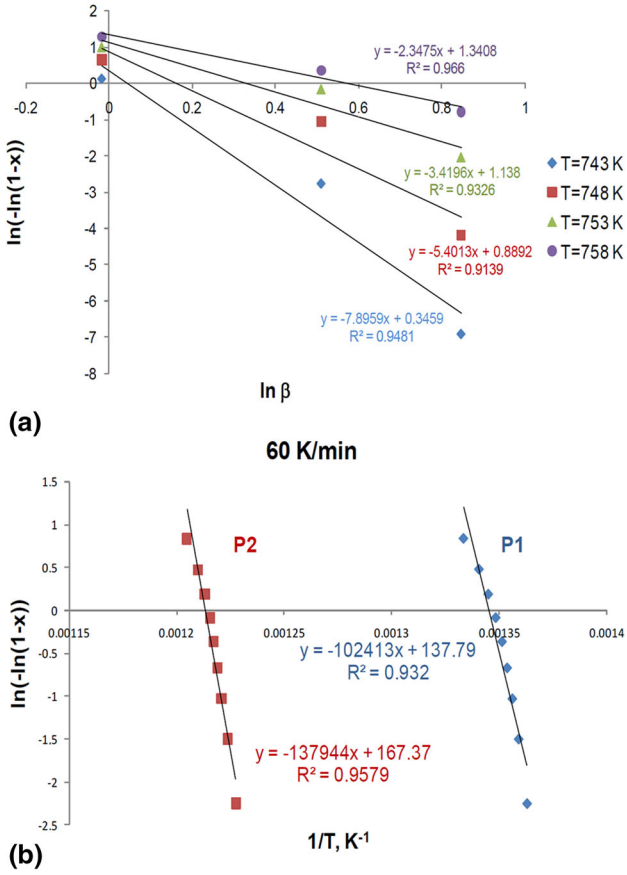

Fig. 12 Determination of n and m parameters for the Matusita–Sakka kinetic model; (a) determination of n parameter as function of heating rate β and temperature T, (b) determination of m parameter for heating rate β 60 K/min. P1—primary crystallization and P2—secondary crystallization peak in the DSC curve

crystallization mechanism including nuclei quenched-in from the liquid phase, followed by the moderate growth.

Another situation concerns secondary crystallization, during which the activation energy increases until the transformed fraction achieves the value corresponding to the peak temperature T_p, and later decreases. Such behavior is especially pronounced when only the CuTi phase appears (Fig. 11b), suggesting that the E_a required for the multi-phase crystallization at the secondary crystallization is much smaller than for the single-phase crystallization. The increase in E_a revealed the increase in the nucleation frequency, in the temperature range up to T_p. This also suggests formation of new nuclei and growth by the mechanism of diffusion in the amorphous phase, retained after primary crystallization. As the amount of amorphous phase decreases, the process requires the increase in E_a to be continued. Similar behavior of E_a was also observed in the kinetic analysis presented in Ref 23.

It should be noticed that the values of activation energy determined by Kissinger method fit very well with the values calculated with the Friedman method, taken as the average values for the properly estimated fractions crystallized at T_p (Fig. 11a and b). Moreover, the value of E_a 288 kJ/mol, reported in Ref 6 for the primary crystallization at moderate rates of heating, agrees well with the present results (Table 2; Fig. 11a).

The Matusita–Sakka method was invented for DSC kinetics investigations for very low heating rates, for the chalcogenide glasses (Ref 15, 16). The method is iso-kinetic and involves double-logarithmic method to calculate the parameters. In spite of many doubts concerning the applicability and the sensitivity of the method (Ref 24), it is quite often used for the studies of BMG's crystallization (Ref 23, 25). As was shown above, the m and n parameters are related to each other. The parameters achieved for the high heating rates used in our DSC experiments are in the range of expectations, except for the primary

Table 5 Values of (n) parameter determined based on the model of Matusita–Sakka (Ref 15, 16)

Peak 1			Peak 2		
T, K	n	n_{av}	T, K	n	n_{av}
743	7.9	4.8	823	6	3.8
748	5.4		828	4.8	
753	3.4		833	2.8	
785	2.3		838	1.8	

n_{av} Average value.

Table 6 Values of (m) parameter, dimensions of growing particles (D) and interpretation of nucleation mechanism determined based on model of Matusita–Sakka (Ref 15, 16)

	Peak 1		Peak 2		$n = m + 1$ or $m = n$	
β, K/min	m	D	m	D	Peak 1	Peak 2
60	3.7	3D?	3.1	3D	$m + 1 = 4.7 = n$ …	$m + 1 = 4.1 \approx n$ No dense nuclei site
100	3.0	3D	2.8	3D	$n > m + 1 = 4.0$ No dense nuclei site	$m = 3.8 = n$ Dense nuclei site
140	2.6	3D	2.7	3D	$n > m + 1 = 3.6$ No dense nuclei site	$m = 3.7 = n$ Dense nuclei site

β Heating rate.

Table 7 Summary of results from analysis of kinetic parameters: heating rates (β), activation energy (E_a), nucleation frequency (Z_{nf}), peak temperature (T_p)

	Friedman/Kissinger—activation energy/reaction	
β, K/min	**Primary crystallization**	**Secondary crystallization**
60-140	Decreasing with transformed fraction $E_a \approx 218$ Small nucleation frequency Z_{nf} (1.3exp(14)); Complex reaction autocatalytic Increase in E_a and Z_{nf} for low β included	Increasing with transformed fraction till T_p $E_a \approx 352$ Large nucleation frequency Z_{nf} (1.7exp(21)); Average E_a and Z_{nf} not sensitive for low β included

	Matusita-Sakka—nucleation and growth			
β, K/min	**Primary crystallization**		**Secondary crystallization**	
60	…	…	No dense nuclei site	3D growth from small dimensions
100	No dense nuclei site	3D growth from small dimensions	Dense nuclei site	3D growth from small dimensions
140	(quenched in)			

crystallization with β 60 K/min. The conclusions, which can be drawn from the parameters, summarized in Table 6, concern 3D growth of particles, which agrees well with the bulk character of the samples. The amorphous matrix does not contain a dense network of nuclei at the start of the crystallization and in the range of primary crystallization particles grow in three dimensions from very small sizes (Table 6). This agrees well with decrease in the E_a calculated by Friedman method and with the relatively small Z_{nf} values for primary crystallization determined by the Kissinger method (Table 2; Fig. 10a). All this suggests the predominant participation of the quenched-in nuclei at that primary stage of crystallization.

The secondary crystallization at the heating rates of 100 and 140 K/min, based on the parameters calculated from the model of Matusita-Sakka, proceeds by growth from small dimensions and from the existing dense lattice of nuclei which does not exist in the range of first DSC peak (Table 6) as results from the n parameter in Matusita–Sakka equation. It suggests that in the range of secondary crystallization, except some amount of the crystalline particles and nuclei supplied by the primary crystallization, also a new nucleation and growth process should proceed, including the new nuclei formation by the diffusion processes. This is in accordance with the E_a evaluation determined by Kissinger method.

All the conclusions from the kinetic parameters look quite reasonable when compared with the results of structural investigations presented in Ref 12-14 and in this paper. According to them, the amorphous phase decomposed into two different compositions in the range of primary crystallization. Relatively small amounts of clusters and nanoparticles crystallized in that temperature range, while a large quantity of the amorphous phase was retained. Even after short-time isothermal annealing at temperatures between the first and the second crystallization peaks in the DSC curves, the amorphous phase partially remained in the structure (Ref 12-14). The TEM observations presented above showed that the secondary crystallization led to the polycrystalline microstructure containing 3D crystals and some amount of the amorphous phase. The summary of the crystallization mechanism, detected from the determination of kinetic parameters and structural investigations, is presented in Table 7.

5. Conclusions

1. Application of the high heating rates, between 60 and 140 K/min in DSC experiments proved to be useful for the determination of crystallization mechanism and the kinetic parameters in CuZrTiPd metallic glass investigations.
2. The XRD and TEM investigations showed that the crystallization process in $Ti_{40}Cu_{36}Zr_{10}Pd_{14}$ BMG with heating/cooling rates between 60 and 140 K/min led to replacing complicated multi-phase crystallization with single CuTi phase.
3. The method of Kissinger of activation energy and nucleation frequency determination for nucleation and growth of the crystalline phase revealed larger E_a and Z_{nf} required for the secondary crystallization than for the primary one in the case of the high heating rates used. The method of Friedman revealed decrease in the activation energy with increased crystallized fraction for the primary crystallization and increase in E_a with transformed fraction in the secondary crystallization.
4. The common E_a values calculated for small and large heating rates suggest that slower, multi-phase crystallization requires larger E_a for the primary crystallization and similar to these for high heating rates for the secondary crystallization.
5. The results of Matusita–Sakka method suggest lack of the dense nuclei site in primary crystallization and dense nuclei site in the secondary one as well as 3D growth of the particles.
6. The conclusions of the kinetic analysis remain in a good agreement with the structural investigations.

Acknowledgments

The work was financed by Grant No. 2013/11/B/ST8/04286 and partially by Grant NN507303940 of the Polish National Scientific Center. The studies were performed in the Accredited Testing Laboratories at the Institute of Metallurgy and Materials Science of the Polish Academy of Sciences.

References

1. A. Inoue and A. Takeuchi, Recent Progress in Bulk Glassy Alloys, *Mater. Trans.*, 2002, **43**, p 1892–1906
2. M. Niinomi, Mechanical Properties of Biomedical Titanium Alloys, *Mater. Sci. Eng. A*, 1998, **243**, p 231–236
3. D. Kuroda, M. Niinomi, M. Morinaga, Y. Kato, and T. Yashiro, Design and Mechanical Properties of New β Type Titanium Alloys for Implant Materials, *Mater. Sci. Eng. A*, 1998, **243**, p 244–249
4. A. Cremasco, W.R. Osoria, C.M.A. Freire, A. Garcia, and R. Caram, Electrochemical Corrosion Behavior of a Ti–35Nb Alloy for Medical Prostheses, *Electrochim. Acta*, 2008, **53**, p 4867–4874
5. S.L. Zhu, X.M. Wang, and A. Inoue, Glass-forming Ability and Mechanical Properties of Ti-based Bulk Glassy Alloys with Large Diameters of up to 1 cm, *Intermetallics*, 2008, **16**, p 1031–1035
6. S.L. Zhu, X.M. Wang, F.X. Qin, and A. Inoue, A New Ti-based Bulk Glassy Alloy with Potential for Biomedical Application, *Mater. Sci. Eng. A*, 2007, **459**, p 233–237
7. S. Zhu, G. Xie, F. Qin, X. Wang, and A. Inoue, Effect of Minor Sn Additions on the Formation and Properties of TiCuZrPd Bulk Glassy Alloy, *Mater. Trans.*, 2012, **53**, p 500–503
8. S.L. Zhu, X.M. Wang, F.X. Qin, M. Yoshimura, and A. Inoue, New TiZrCuPd Quaternary Bulk Glassy Alloys with Potential of Biomedical Applications, *Mater. Trans.*, 2007, **48**, p 2445–2448
9. S.L. Zhu, X.M. Wang, G.Q. Xie, F.X. Qin, M. Yoshimura, and A. Inoue, Formation of Ti-based Bulk Glassy Alloy/Hydroxyapatite Composite, *Scr. Mater.*, 2008, **58**, p 287–290
10. F.X. Qin, X.M. Wang, G.Q. Xie, and A. Inoue, Distinct Plastic Strain of Ni-free Ti–Zr–Cu–Pd–Nb Bulk Metallic Glasses with Potential for Biomedical Applications, *Intermetallics*, 2008, **16**, p 1026–1030
11. T.G. Nieh, *Deformation Behavior, Bulk Metallic Glases*, M. Miller and P. Liaw, Ed., Springer, New York, 2008, p 147–167
12. A. Sypien, Observation of the Complex Local Crystallization Process in Ti–Zr–Cu–Pd Amorphous Ribbons and Bulk Metallic Glass, *Arch. Metall. Mater.*, 2013, **58**, p 347–350
13. A. Sypien, T. Czeppe, G. Garzel, L. Litynska, J. Latuch, and N.Q. Chinh, Thermal Stability and Mechanical Properties of the TiCuZrPd Glasses with 10, 14 and 20 at.% Pd, *J. Alloy. Compd.*, 2014, **615**, p 108–112
14. A. Sypien, M. Stoica, and T. Czeppe, Properties of the $Ti_{40}Zr_{10}Cu_{36}Pd_{14}$ BMG Modified by Sn and Nb Additions, *J. Mater. Eng. Perform.*, 2016, **25**, p 800–808
15. K. Matusita and S. Sakka, Kinetic Study on Crystallization of Glass by Differential Thermal Analysis-Criterion on Application of Kissinger Plot, *J. Non-Cryst. Solids*, 1980, **38–39**, p 741–746
16. K. Matusita, T. Komatsu, and R. Kokota, Kinetics of Non-isothermal Crystallization Process and Activation Energy for Crystal Growth in Amorphous Materials, *J. Mater. Sci.*, 1984, **19**, p 291–296
17. A. Sypien and W. Przybylo, Preparation of Ti–Ni–Fe Phase by Levitation and Its Structural Characterization, *J. Mater. Sci. Technol.*, 2010, **26**, p 31–35
18. R.J. Furlan, G. Bambakidis, J.S. Cantrell, R.C. Bowman, Jr., and A.J. Mealand, Thermal Stabilities of the Crystalline and Amorphous Ti_yCuH_x Systems, *J. Less-Common Met.*, 1986, **116**, p 375–388
19. D. Nataraj, K. Prabakar, S.K. Narayandass, and D. Mangalaraj, Determination of Kinetic Parameters of Bi_2Se_3 Thin Films by Computation, *Cryst. Res. Technol.*, 2000, **35**, p 1087–1094
20. M. Shapaan, J. Lábár, J. Lendvai, and L.K. Varga, Crystallization Behavior of $Fe_{62}Nb_8 - xZr_xB_{30}$ Bulk Amorphous Alloy, *Mater. Sci. Eng. A*, 2004, **375–377**, p 789–793
21. H.E. Kissinger, Reaction Kinetics in Differential Thermal Analysis, *Anal. Chem.*, 1957, **29**, p 1702–1706
22. H.L. Friedman, Kinetics of Thermal Degradation of Char-forming Plastics from Thermogravimetry. Application to a Phenolic Plastic, *J. Polym. Sci. Polym. Symp.*, 1964, **6**, p 183–195
23. S.R. Prajapati, S. Kasyap, A.T. Patel, and A. Pratap, Non-isothermal Crystallization Kinetics of $Zr_{52}Cu_{18}Ni_{14}Al_{10}Ti_6$ Metallic Glass, *J. Therm. Anal. Calorim.*, 2016, **124**, p 21–33
24. J. Malek, Kinetic Analysis of Crystallization Processes in Amorphous Materials, *Thermochim. Acta*, 2000, **355**, p 239–253
25. J.S.C. Jang, S.F. Tsao, L.J. Chang, J.C. Huang, and C.T. Liu, Nanocrystallization of $Zr_{61}Al_{7.5}Cu_{17.5}Ni_{10}Si_4$ Metallic Glass, *Intermetallics*, 2009, **17**, p 56–64
26. K. Hono, D.H. Ping, M. Ohnuma, and H. Onodera, Cu Clustering and Si Partitioning in the Early Crystallization Stage of an $Fe_{73.5}Si_{13.5}B_9Nb_3Cu_1$ Amorphous Alloy, *Acta Mater.*, 1999, **47**(3), p 997–1006